Galactic winds with MUSE: A direct detection of Fe ii* emission from a z = 1.29 galaxy

Hayley Finley, Nicolas Bouche, Thierry Contini, Benoit Epinat, Roland Bacon, Jarle Brinchmann, Sebastiano Cantalupo, Santiago Erroz-ferrer, Raffaella Anna Marino, Michael Maseda, et al.

A&A 605, A118 (2017)
DOI: 10.1051/0004-6361/201730428

Astronomy & Astrophysics

Galactic winds with MUSE: A direct detection of Fe II* emission from a $z = 1.29$ galaxy⋆

Hayley Finley[1,2], Nicolas Bouché[3], Thierry Contini[1,2], Benoît Epinat[1,2,4], Roland Bacon[5], Jarle Brinchmann[6,7], Sebastiano Cantalupo[8], Santiago Erroz-Ferrer[8], Raffaella Anna Marino[8], Michael Maseda[6], Johan Richard[5], Ilane Schroetter[1,2], Anne Verhamme[5,9], Peter M. Weilbacher[10], Martin Wendt[10,11], and Lutz Wisotzki[10]

[1] Université de Toulouse, UPS-OMP, 31400 Toulouse, France
e-mail: hayley.finley@irap.omp.eu
[2] IRAP, Institut de Recherche en Astrophysique et Planétologie, CNRS, 14 avenue Édouard Belin, 31400 Toulouse, France
[3] IRAP, Institut de Recherche en Astrophysique et Planétologie, CNRS, 9 avenue Colonel Roche, 31400 Toulouse, France
[4] Aix-Marseille Univ, CNRS, LAM, Laboratoire d'Astrophysique de Marseille, Marseille, France
[5] CRAL, Observatoire de Lyon, CNRS, Université Lyon 1, 9 avenue Ch. André, 69561 Saint-Genis Laval Cedex, France
[6] Leiden Observatory, Leiden University, PO Box 9513, 2300 RA Leiden, The Netherlands
[7] Instituto de Astrofísica e Ciências do Espaço, Universidade do Porto, CAUP, Rua das Estrelas, 4150-762 Porto, Portugal
[8] ETH Zurich, Institute of Astronomy, Wolfgang-Pauli-Str. 27, 8093 Zürich, Switzerland
[9] Observatoire de Genève, Université de Genève, 51 Ch. des Maillettes, 1290 Versoix, Switzerland
[10] Leibniz-Institut für Astrophysik Potsdam (AIP), An der Sternwarte 16, 14482 Potsdam, Germany
[11] Institut für Physik und Astronomie, Universität Potsdam, Karl-Liebknecht-Str. 24/25, 14476 Golm, Germany

Received 12 January 2017 / Accepted 31 May 2017

ABSTRACT

Emission signatures from galactic winds provide an opportunity to directly map the outflowing gas, but this is traditionally challenging because of the low surface brightness. Using very deep observations (27 h) of the *Hubble* Deep Field South with the Multi Unit Spectroscopic Explorer (MUSE) instrument, we identify signatures of an outflow in both emission and absorption from a spatially resolved galaxy at $z = 1.29$ with a stellar mass $M_\star = 8 \times 10^9\ M_\odot$, star formation rate $SFR = 77^{+40}_{-25}\ M_\odot\ \mathrm{yr}^{-1}$, and star formation rate surface brightness $\Sigma_{\rm SFR} = 1.6\ M_\odot\ \mathrm{kpc}^{-2}$ within the [O II] $\lambda\lambda$3727, 3729 half-light radius $R_{1/2,[\rm OII]} = 2.76 \pm 0.17$ kpc. From a component of the strong resonant Mg II and Fe II absorptions at -350 km s^{-1}, we infer a mass outflow rate that is comparable to the star formation rate. We detect non-resonant Fe II* emission, at λ2365, λ2396, λ2612, and λ2626, at $1.2{-}2.4{-}1.5{-}2.7 \times 10^{-18}$ erg s^{-1} cm^{-2} respectively. The flux ratios are consistent with the expectations for optically thick gas. By combining the four non-resonant Fe II* emission lines, we spatially map the Fe II* emission from an individual galaxy for the first time. The Fe II* emission has an elliptical morphology that is roughly aligned with the galaxy minor kinematic axis, and its integrated half-light radius, $R_{1/2,\rm Fe\,II*} = 4.1 \pm 0.4$ kpc, is 70% larger than the stellar continuum ($R_{1/2,\star} \simeq 2.34 \pm 0.17$) or the [O II] nebular line. Moreover, the Fe II* emission shows a blue wing extending up to -400 km s^{-1}, which is more pronounced along the galaxy minor kinematic axis and reveals a C-shaped pattern in a $p - v$ diagram along that axis. These features are consistent with a bi-conical outflow.

Key words. galaxies: evolution – galaxies: formation – galaxies: starburst – galaxies: ISM – ISM: jets and outflows – ultraviolet: ISM

1. Introduction

Galactic winds, driven by the collective effect of hot stars and supernovae explosions, play a major role in regulating galaxy evolution. By expelling enriched matter beyond the halo, galactic winds can address discrepancies between observations and ΛCDM models that over-predict the number of low-mass galaxies (Silk & Mamon 2012) and enrich the intergalactic medium (Oppenheimer & Davé 2008; Cen & Chisari 2011; Shen et al. 2012; Pallottini et al. 2014; Rahmati et al. 2016; Ford et al. 2016). Likewise, galactic winds may play a major role in regulating the mass-metallicity relation (Finlator & Davé 2008; Lilly et al. 2013; Tremonti et al. 2004). Therefore, quantifying the mass fluxes of galactic outflows (and their extents) is necessary to gain a complete understanding of galaxy evolution.

However, while galactic winds appear ubiquitous (e.g., Veilleux et al. 2005; Weiner et al. 2009; Steidel et al. 2010; Rubin et al. 2010b, 2014; Martin et al. 2012; Heckman et al. 2015; Zhu et al. 2015; Chisholm et al. 2015; Gallerani et al. 2016; Fiore et al. 2017), observational constraints for the physical properties of galactic outflows, including their extents and mass outflow rates, are sparse. Traditional "down the barrel" 1D galaxy spectroscopy provides direct constraints on the wind speed from the blue-shifted absorption lines but cannot constrain the physical extent of outflows, leading to large uncertainties in outflow rates. Techniques that use a background source can address this question.

For instance, the background quasar technique provides constraints on the physical extent of gas flows from the impact parameter between the galaxy and the absorbing gas (e.g., Bouché et al. 2012, 2016; Kacprzak et al. 2012; Schroetter et al. 2015, 2016; Péroux et al. 2016; Straka et al. 2016). These recent studies have made progress investigating the kinematics, orientation, and extent of gas flows around star forming galaxies.

⋆ Based on observations of the *Hubble* Deep Field South made with ESO telescopes at the La Silla Paranal Observatory under program ID 60.A-9100(C). Advanced data products are available at http://muse-vlt.eu/science

As a variation on this technique, spectroscopy against a background galaxy probes absorption from the foreground galaxy halo over a larger solid angle (e.g., Adelberger et al. 2005; Rubin et al. 2010a; Steidel et al. 2010; Bordoloi et al. 2011, 2014; Diamond-Stanic et al. 2016). However, these constraints on the physical extent of outflows are usually limited due to their 1D nature, except for Cazzoli et al. (2016). Mapping the extent of gas flows in 2D is critical to better constrain mass outflow rates.

Mapping outflows in emission, such as for M82 (e.g., Shopbell & Bland-Hawthorn 1998; Lehnert et al. 1999) and other nearby galaxies (e.g., Heckman et al. 1995; Cecil et al. 2001; Veilleux & Rupke 2002; Matsubayashi et al. 2009; Moiseev et al. 2010; Bolatto et al. 2013; Krips et al. 2016), is difficult at high redshift, because the emitting gas inherently has a very low surface brightness. Nonetheless, several studies have detected emission signatures from outflows in galaxies beyond the local universe (e.g., Genzel et al. 2011; Newman et al. 2012; Förster Schreiber et al. 2014). Currently, rest-frame UV and optical spectroscopy use three types of emission signatures to map the extent of outflows: the nebular, resonant, and non-resonant emission lines.

The most common nebular emission lines seen in H II regions are hydrogen recombination and forbidden lines, such as [O II] $\lambda\lambda$ 3727, 3729. A transition is resonant when a photon can be absorbed from the ground state and re-emitted to the same lowest level of the ground state, as for Lyman-alpha and the Mg II $\lambda\lambda$2796, 2803 transitions. A transition is non-resonant when the photon can be re-emitted to an excited level of a ground state that has multiple levels due to fine structure splitting. Non-resonant transitions are commonly denoted with a *, like Fe II*. Due to the slight energy difference between the ground and excited states, photons from non-resonant emission no longer have the correct wavelength to be re-absorbed through a resonant transition and instead escape. In other words, the gas is optically thin to photons that are emitted through a non-resonant transition.

The first type of emission signature (nebular lines) from outflows can appear as a broad component in nebular emission lines such as Hα. Broad components are regularly seen in local ultra-luminous infra-red galaxies (ULIRGs, e.g., Soto & Martin 2012; Arribas et al. 2014; García-Burillo et al. 2015) and more recently in normal star-forming galaxies (Wood et al. 2015; Cicone et al. 2016). At high redshifts, Newman et al. (2012) detected a broad Hα component in composite spectra of $z \sim 2$ star-forming galaxies and Genzel et al. (2011) observed this broad component in star-forming clumps from a few individual galaxies. Similarly, Förster Schreiber et al. (2014) measure broad Hα and [N II] components from AGN-driven outflows in seven individual $z \sim 2$ galaxies. While the broad component from the AGN-driven outflows presented in Förster Schreiber et al. (2014) is localized near the galaxy nuclei, Newman et al. (2012) found that the broad emission is spatially extended beyond the half-light radius, $R_{1/2}$.

The second possible emission signature of outflows comes from resonant transitions. A common resonant line is Lyα, and deep surveys have shown that Lyα is often more extended than the stellar continuum (e.g., Steidel et al. 2011; Matsuda et al. 2012; Wisotzki et al. 2016) but can be strongly affected by dust absorption because of its large optical depth (Laursen et al. 2009). Emission from resonant metal lines, such as Na I D, Si II, Fe II, or Mg II, is less affected by dust than Lyα and may be observed as P-cygni profiles (e.g., Erb et al. 2012; Rupke & Veilleux 2015; Scarlata & Panagia 2015). The relative strength between the (mostly) blue-shifted absorption and (mostly) redshifted emission dictates whether the signature appears as a traditional P-cygni profile or as emission "infilling". The impact of emission infilling varies for different transitions, as discussed in Tang et al. (2014) and Zhu et al. (2015). Contrary to the resonant Fe II lines observed across a similar wavelength range (Fe II λ2344, $\lambda\lambda$2374, 2382, and $\lambda\lambda$2586, 2600), the Mg II $\lambda\lambda$2796, 2803 doublet is particularly sensitive to emission infilling, since its lower energy level does not have fine structure splitting. As a result of the different possible relative strengths of the emission and absorption components, observed profiles for the resonant Mg II $\lambda\lambda$2796, 2803 transitions vary greatly for different star-forming galaxies (Weiner et al. 2009; Rubin et al. 2011; Coil et al. 2011; Erb et al. 2012; Talia et al. 2012; Martin et al. 2012, 2013; Kornei et al. 2013).

The third possible signature of outflows in emission is from non-resonant transitions such as C II*, Si II* (e.g., Shapley et al. 2003) or Fe II* (e.g., Rubin et al. 2011). Detecting non-resonant emission typically requires stacking hundreds of galaxy spectra. Using more than 800 Lyman break galaxies (LBGs) at $z > 2$, Shapley et al. (2003) first detected Si II* in the composite spectrum, and Berry et al. (2012) more recently detected C II* and Si II* in the composite spectrum of 59 LBGs. Since the non-resonant Fe II* lines are at redder wavelengths than C II* and Si II*, they are practical for investigating outflows at lower redshifts, like $z \sim 1$. Based on comparing composite spectra from samples of ~100 or more star-forming galaxies at $z \sim 1-2$ (Erb et al. 2012; Kornei et al. 2013; Tang et al. 2014), Fe II* emission may vary with galaxy properties, such as galaxy mass and dust attenuation. Coil et al. (2011) present individual spectra with different combinations of blue-shifted absorption, resonant Mg II emission, and non-resonant Fe II* emission. In two notable direct detections of Fe II* emission from galaxies at $z = 0.694$ and $z = 0.9392$ (Rubin et al. 2011; Martin et al. 2012), the non-resonant emission is observed along with blue-shifted absorption lines and resonant Mg II emission, allowing the authors to constrain and model the outflows. Similarly, Jaskot & Oey (2014) use non-resonant C II* and Si II* emission in UV spectra of four green pea galaxies at $z \sim 0.14-0.2$ to infer the geometry of their outflows.

These studies provide information about outflow properties on galactic scales, but it is also possible to characterize outflows from individual star-forming regions across $z > 1$ galaxies thanks to adaptive optics or gravitational lensing (i.e., Genzel et al. 2011; Rigby et al. 2014; Karman et al. 2016; Bordoloi et al. 2016; Patricio et al., in prep.). Using adaptive optics, Genzel et al. (2011) identify star-forming regions in five $z > 2$ galaxies and argue that bright regions (or clumps) with a broad component in the nebular emission are the launch sites for massive galactic winds. With the benefit of gravitational lensing, Karman et al. (2016) characterize Mg II emission, Fe II* $\lambda\lambda$2612, 2626 emission, and Fe II absorption from multiple star-forming regions across a supernova host galaxy at $z = 1.49$ at locations both associated with and independent of the supernovae explosion. Bordoloi et al. (2016) likewise detect blue-shifted Fe II and Mg II absorptions, redshifted Mg II emission, and non-resonant Fe II* $\lambda\lambda$2612, 2626 emission in four star-forming regions of a gravitationally lensed galaxy at $z = 1.70$ but find that the outflow properties vary from region to region. Spatially resolved observations suggest that outflow properties could be localized and strongly influenced by the nearest star-forming clump.

Despite advances from these diverse studies, we have not yet been able to map the morphology and extent of outflows driven by star formation from individual galaxies beyond the local

universe. The new generation of integral field spectrographs, the Multi Unit Spectroscopic Explorer (MUSE; Bacon et al. 2015) on the VLT and the Keck Cosmic Web Imager (Morrissey et al. 2012), are well suited for studying galactic winds in emission and tackling this challenge. While slit spectroscopy can inadvertently miss scattered emission if the aperture does not cover the full extent of the outflowing envelope (Scarlata & Panagia 2015), integral field observations eliminate aperture effects for distant galaxies, making emission signatures easier to detect. The combined spatial and spectroscopic data facilitate characterizing the morphology and kinematics of both star-forming galaxies and the outflows they produce.

In this paper, we analyze galactic wind signatures from a spatially resolved star-forming galaxy at $z = 1.2902$ observed with MUSE. We present the observations in Sect. 2 and summarize the galaxy properties in Sect. 3. With the integrated 1D MUSE galaxy spectrum, we characterize outflow signatures from Fe II, Mg II, and Mg I transitions in absorption and Fe II* transitions in emission in Sect. 4. We then investigate the spatial extent and the kinematic properties of the Fe II* emission in Sects. 5 and 6, respectively. In Sect. 7, we compare our observations with radiative transfer wind models and estimate the mass outflow rate. We review our findings in Sect. 8. Throughout the paper, we assume a ΛCDM cosmology with $\Omega_m = 0.3$, $\Omega_\Lambda = 0.7$, and $H_0 = 70$ km s^{-1} Mpc^{-1}. With this cosmology, 1 arcsec corresponds to 8.37 kpc at the redshift of the galaxy.

2. Data

MUSE fully covers the wavelength range 4650–9300 Å with 1.25 Å per spectral pixel. The field of view spans $1' \times 1'$ with a pixel size of $0.2''$. The instrument is notable both for its high throughput, which reaches 35% at 7000 Å (end-to-end including the telescope), and its excellent image quality sampled at $0.2''$ per spaxel. While MUSE provides new possibilities for addressing a wide variety of scientific questions, these two characteristics make the instrument optimal for deep field observations.

As part of commissioning data taken during July and August 2014, MUSE observed a $1' \times 1'$ field of view in the *Hubble* Deep Field South (HDFS) for a total integration time of 27 h. The final data cube was created from a 5σ-clipped mean of 54 individual exposures that were taken in dark time under good seeing conditions ($0.5''-0.9''$). The 1σ emission-line surface brightness limit for this cube is 1×10^{-19} erg s^{-1} cm^{-2} arcsec^{-2}. The MUSE observations provided spectroscopic redshifts for 189 sources with magnitude $I_{814} \leq 29.5$ (8 stars and 181 galaxies), a factor-often increase over the 18 previously-measured spectroscopic redshifts in this field. A catalog of sources in the MUSE HDFS field includes the redshifts, emission-line fluxes, and 1D spectra. The observations, the data cube, and an overview of scientific exploitations are fully described in Bacon et al. (2015). Both the data cube and the catalog of sources are publicly available[1].

The deep IFU observations reveal emission from Fe II* transitions directly detected from one galaxy in the MUSE HDFS. The galaxy has ID #13 in the MUSE catalog, with coordinates $\alpha = 22^h\,32^m\,52.16^s$, $\delta = -60°33'23.92''$ (J2000) and magnitude $I_{814} = 22.83 \pm 0.005$. It is part of a nine-member group at $z \simeq 1.284$, discussed in Bacon et al. (2015), which also includes two AGN and an interacting system with tidal tails. This direct detection of a galaxy with Fe II* emission offers a new opportunity to characterize galactic winds.

[1] http://muse-vlt.eu/science/hdfs-v1-0/

3. Galaxy properties

Galaxy ID#13 is part of a sample of 28 spatially resolved galaxies that Contini et al. (2016) selected from the MUSE HDFS according to the criterion that the brightest emission line covers at least 20 spatial pixels with a signal-to-noise ratio (S/N) higher than 15. For this galaxy, emission from the [O II] $\lambda\lambda$3727, 3729 doublet is the dominant feature in the MUSE spectrum. We determined the galaxy systemic redshift from a *p-v* diagram extracted from the MUSE data cube along the galaxy kinematic major axis by fitting a double Gaussian profile to the [O II] $\lambda\lambda$3727, 3729 emission at each position along the slit. The systemic redshift of $z = 1.29018 \pm 0.00006$ is the mean value between the two asymptotes of the rotation curve.

Contini et al. (2016) investigated the morphological and kinematic properties of the galaxy ID#13, as part of the MUSE HDFS spatially resolved galaxy sample. They constrained the morphology from HST images in the F814W band by modeling the galaxy with GALFIT (Peng et al. 2002) as a bulge plus an exponential disk. Contini et al. (2016) then performed the kinematic analysis with two different techniques: a traditional 2D line-fitting method with the Camel algorithm (Epinat et al. 2012; Contini et al. 2016) combined with a 2D rotating disk model, which requires prior knowledge of the galaxy inclination, and a 3D fitting algorithm, GalPaK^{3D} (Bouché et al. 2015), which simultaneously fits the morphological and kinematic parameters directly from the MUSE data cube. The parameters from the 2D and 3D models are in good agreement overall (see Table 1).

From the morphological analysis on the HST images, we find that galaxy ID#13 is compact with a disk scale length of $R_d = 1.25$ kpc (correspondingly $R_{1/2} = 2.1$ kpc) and has a low inclination angle of $i = 33°$. The inclination from 3D fitting yields a lower value of ∼20°. The disagreement likely arises from an asymmetric morphology seen in the HST images, since statistically the two techniques measure inclinations that are in good agreement (Contini et al. 2016). The galaxy also shows a misalignment between the morphological position angle measured from the HST image, −46°, and the MUSE kinematic position angle, −13°, again likely due to the asymmetric light distribution that only appears at higher spatial resolution. Regardless, the galaxy has a low inclination with $i \sim 20°-30°$.

From the kinematic analysis on the MUSE data, the velocity field has a low gradient, ±10 km s^{-1}, a low maximum velocity, 24 km s^{-1}, and a velocity dispersion of 45–50 km s^{-1}. Therefore, non-circular motions dominate the gas dynamics within the disk, with $V/\sigma \approx 0.5$, that is, below the commonly-used $V/\sigma \leq 1$ threshold for identifying dispersion-dominated galaxies. We note that the different maximum velocities from the 2D and 3D methods are entirely due to the different inclination values (Table 1). Nonetheless, the ratio remains $V/\sigma \lesssim 1$ for the range of possible inclinations, 17°–33°.

Contini et al. (2016) estimated the visual extinction, $A_V = 1.20$ mag, stellar mass, $M_\star = 8 \times 10^9\ M_\odot$, and star formation rate $SFR = 77^{+40}_{-25}\ M_\odot$ yr^{-1}, from stellar population synthesis using broadband visible and near infra-red photometry[2]. The galaxy ID#13 is one of the most massive of the 28 spatially-resolved galaxies in the MUSE HDFS sample and also has the highest star formation rate (SFR). This SFR places galaxy ID#13 above the main sequence (Elbaz et al. 2007; Karim et al. 2011; Whitaker et al. 2014; Tomczak et al. 2016) by almost 1 dex, indicating that this galaxy is undergoing a starburst with a high

[2] The [OII]-derived SFR for a Chabrier (2003) IMF is 65 $M_\odot$ yr^{-1} using the Kewley et al. (2004) calibration, which also yields an extinction of $A_V = 1.5$ in the gas.

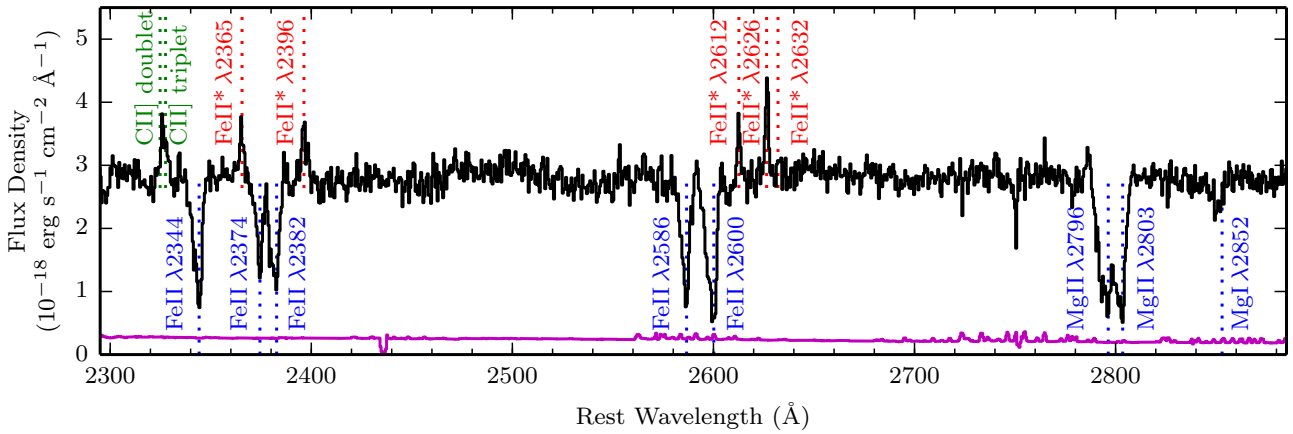

Fig. 1. Vacuum rest-frame 1D spectrum of the MUSE HDFS galaxy ID#13 covering the Fe II and Mg II transitions. The spectrum is in black with the 1σ error in magenta. Resonant transitions detected in absorption are labeled in blue. Non-resonant Fe II* transitions detected in emission are labeled in red. The C II] nebular emission, which is a blend of five transitions, is labeled in green.

Table 1. Galaxy ID#13 properties from Contini et al. (2016).

Morphological analysis	HST + GALFIT
Position angle (°)	-45.9 ± 1.9
Inclination i (°)	33 ± 5
Half-light radius (kpc)	2.1 ± 0.03
Kinematic analysis	**MUSE 2D/3D**
Position angle (°)	−14/−13
Inclination i (°)	+28/+17
Max. rotational velocity (km s^{-1})	+24/+44
Velocity dispersion (km s^{-1})	+48/+46
Photometric analysis	**SED fitting**
Visual extinction A_V (mag)	$1.20^{+0.59}_{-0.26}$
$\log(M_\star)$ ($M_\odot$)	9.89 ± 0.11
$\log$(SFR) ($M_\odot$ yr^{-1})	1.89 ± 0.18

specific SFR of sSFR = 10 Gyr^{-1}. The starburst phase of galaxy evolution can produce large-scale outflows when many short-lived massive stars explode as supernovae.

The properties of this galaxy are conducive to detecting signatures from galactic winds. The low inclination angle favors observing blue-shifted absorptions, given that this signature increases substantially toward face-on galaxies (Chen et al. 2010; Kornei et al. 2012; Rubin et al. 2014). The [O II] luminosity (~10^{43} erg s^{-1}) and rest-frame equivalent width (~50 Å, see Table 3) indicate that the galaxy ID#13 is also well-suited for investigating winds in emission, since Fe II* and Mg II emission correlate with $L_{\rm O\,II}$ or [O II] rest-frame equivalent width (Kornei et al. 2013; Zhu et al. 2015).

4. Absorption and emission profiles from the 1D spectrum

In this section, we analyze the galaxy ID#13 1D spectrum extracted from the MUSE data using a white-light weighting scheme. The 1D MUSE spectrum (Fig. 1) reveals resonant Fe II, Mg II, and Mg I self-absorption, non-resonant Fe II* emission, and C II] and [O II] nebular emission lines. The Fe II transitions occur in three multiplets[3]. In the Fe II UV1, UV2, and UV3 multiplets, a photon can be re-emitted either through a resonant transition to the ground state, which produces emission infilling, or through a non-resonant transition to an excited state in the lower level, in which case the emission occurs at a slightly different wavelength. We investigate the integrated absorption and emission profiles, focusing first on the resonant absorption and emission properties (Sect. 4.1), then on the non-resonant emission properties (Sect. 4.2).

4.1. Resonant Fe and Mg profiles

Figure 2 presents the velocity profiles of each of the individual Fe II, Mg II, and Mg I transitions relative to the galaxy systemic redshift, for comparison. The self-absorption profiles are asymmetric, with the strongest component centered on the galaxy systemic redshift, and a significant blue wing extending to −800 km s^{-1}. We fit these profiles simultaneously with VPFIT[4] v10, using several components and requiring each to have the same redshift and Doppler parameter across the different transitions. The absorptions are well fit with three components at redshifts 1.28514 ± 0.00021, 1.28752 ± 0.00009, and 1.29024 ± 0.00006, corresponding to shifts of -660 ± 28 km s^{-1}, -349 ± 12 km s^{-1} and $+8.5 \pm 6.5$ km s^{-1} relative to the galaxy systemic velocity. Table 2 summarizes the total rest-frame equivalent widths for each transition, calculated both from the fit and directly from the flux.

Globally, the Fe II resonant transitions in Fig. 2 reveal several key features: (1) the Fe II profiles are very similar to one another, and (2) the strongest component is roughly centered at the galaxy systemic redshift. As Prochaska et al. (2011) first demonstrated, emission infilling in resonant absorption lines can alter doublet ratios and mimic partial coverage. However, here we find that emission infilling does not play a significant role in this galaxy for the following two qualitative arguments.

First, while strong emission infilling would produce clear P-cygni profiles (which are not observed), moderate amounts of emission infilling would cause a blue-shift to the centroid of the absorption, an effect commonly seen in stacked spectra (e.g., Zhu et al. 2015) or individual cases (Rubin et al. 2011; Martin et al. 2013). None of the absorptions in the galaxy ID#13 spectrum (Fig. 2) have blue-shifted centroids.

Second, because Fe II has multiple channels to re-emit the photons (through resonant and non-resonant transitions), the

[3] See Tang et al. (2014) or Zhu et al. (2015) for energy level diagrams.

[4] http://www.ast.cam.ac.uk/~rfc/vpfit.html

Table 2. Absorption rest-frame equivalent widths for the three sub-components in Fig. 2.

Components		A	B	C	Total	
Redshift		1.28514	1.28752	1.29024		
Δv (km s^{-1})		-660 ± 28	-349 ± 12	$+8.5 \pm 6.5$		
Transition	Multiplet	$W_{0,\mathrm{fit}}$ (Å)	$W_{0,\mathrm{fit}}$ (Å)	$W_{0,\mathrm{fit}}$ (Å)	$W_{0,\mathrm{fit}}$ (Å)	$W_{0,\mathrm{flux}}$ (Å)
(1)	(2)	(3)	(4)	(5)	(6)	(7)
Fe II λ2344	Fe II UV3	0.13	0.93	2.06	3.09	3.47 ± 0.24
Fe II λ2374	Fe II UV2	0.04	0.55	1.70	2.42	2.20 ± 0.22
Fe II λ2382	Fe II UV2[a]	0.24	1.17	2.36	3.69	3.27 ± 0.22
Fe II λ2586	Fe II UV1	0.10	0.91	2.15	3.14	3.14 ± 0.26
Fe II λ2600	Fe II UV1	0.24	1.24	2.52	3.97	4.28 ± 0.25
Mg II λ2796		0.98	1.64	2.82	5.51	5.09 ± 0.18
Mg II λ2803		0.93	1.89	2.63	4.47	4.90 ± 0.17
Mg I λ2853		0.16	0.49	0.31	0.94	0.86 ± 0.21

Notes. Column (1): absorption line. Column (2): Multiplet associated with transition. Column (3): equivalent width for component A. Column (4): equivalent width for component B. Column (5): equivalent width for component C. Column (6): total equivalent width measured from fits. Column (7): total equivalent width measured from the spectrum. [(a)] Fe II λ2382 is a pure resonant absorption line with no associated Fe II* emission.

degree of infilling for a particular Fe II absorption line depends on the likelihood of re-emission through the different channels within a multiplet. Purely resonant transitions, such as Mg II and Fe II λ2382, are the most sensitive to emission infilling. Zhu et al. (2015) demonstrated that the Fe II resonant absorptions that are the least (most) affected by emission infilling are Fe II λ2374 (Fe II λ2600 and Fe II λ2382) respectively. Figure 2 shows that the Fe II λ2374, λ2600 and λ2382 absorption profiles are all very similar for the galaxy ID#13. The lack of blue-shifted centroids and the consistent absorption profiles suggest that emission infilling does not have a strong impact.

We quantify (and put a limit on) the global amount of infilling using the method proposed by Zhu et al. (2015), which consists of comparing the observed rest-frame equivalent widths of the resonant lines to those seen in intervening quasar spectra (see their Fig. 12). Using the averaged rest-frame equivalent widths of resonant Fe II and Mg II absorptions from a stacked spectrum of ~30 strong Mg II absorber galaxies at $0.5 < z < 1.5$ from Dutta et al. (2017, their Table 7), we find that our data could allow for at most <0.9 Å (<1.9 Å) of infilling for Fe II λ2600 (Fe II λ2382), the two transitions most susceptible to infilling (Zhu et al. 2015). This means that at most 22% (55%) of these absorptions could be affected by infilling and that the impact on the other Fe II absorptions is even smaller.

In addition, we can estimate the amount of infilling for each of the three sub-components shown in Fig. 2 (Table 2). We are unable to put constraints on the weak component "A", but the blue-shifted component "B" at -350 km s^{-1} does not allow for emission infilling that would increase the Fe II λ2382 equivalent width by more than 10%. The component "C" at the galaxy systemic redshift allows for the largest amount of emission infilling with 60% corrections for Fe II λ2600 and Fe II λ2382, 40% for Fe II λ2344 and 20% for Fe II λ2586. As we discuss later in Sect. 7.2, the blue-shifted galactic wind component ("B") appears to be less affected by emission infilling than the systemic component associated with the galaxy interstellar medium (ISM), ("C").

We end this section by mentioning that, as we will argue in Sect. 7.2, the Fe II and Mg II gas is likely optically thick. The absorptions ought to be saturated, and the reason we do not observe fully absorbed profiles is either because of a partial covering fraction (rather than emission infilling) or more likely the low spectral resolution. As we will show in the next section, the non-resonant Fe II* emission pattern is also consistent with optically thick gas.

4.2. Non-resonant emission

Figure 3 shows the non-resonant transitions Fe II* λ2365, λ2396, λ2612, and λ2626 that we detect in the MUSE HDFS galaxy ID#13 1D spectrum at 2.5σ–6σ significance. No Fe II* λ2632 emission is detected (Fig. 1). The fluxes in the non-resonant transitions Fe II* λ2365, λ2396, λ2612, λ2626 transitions are 1.2–2.4–1.5–2.7×10^{-18} erg s^{-1} cm^{-2}, respectively. Table 3 gives the emission peak fluxes and rest-frame equivalent widths measured for all of the Fe II* transitions. These flux ratios of 0.5:1.0:0.6:1.0 are consistent with the expectation (0.66:1.0:0.66:1.0) for optically thick gas discussed in Tang et al. (2014). In the optically thin regime, the flux ratios should be on the order of approximately one.

Regarding the non-detection of Fe II* λ2632, we note that this transition is usually not detected in stacked spectra (Talia et al. 2012; Kornei et al. 2013; Tang et al. 2014; Zhu et al. 2015), except for in the Erb et al. (2012) stacked spectrum, but that it is observed in the other individual cases (Rubin et al. 2011; Martin et al. 2013). Tang et al. (2014) explore whether underlying stellar absorption suppresses the Fe II* λ2632 emission in their stacked spectra. However, for this starburst galaxy, the F- and G-type stars that produce the underlying absorption are unlikely to significantly contribute to the stellar continuum.

We perform a joint Gaussian fit to the four non-resonant Fe II* emission peaks and find that they appear symmetric and centered on the galaxy systemic redshift measured from [O II] $\lambda\lambda$3727, 3729 (Fig. 3). This is in contrast to Zhu et al. (2015), who found that the Fe II* emission from their stacked spectrum of 8600 galaxies is slightly asymmetric, and in contrast to Rubin et al. (2011), who observed Fe II* emission peaks that are slightly (~30 km s^{-1}) redshifted relative to the nebular emission lines.

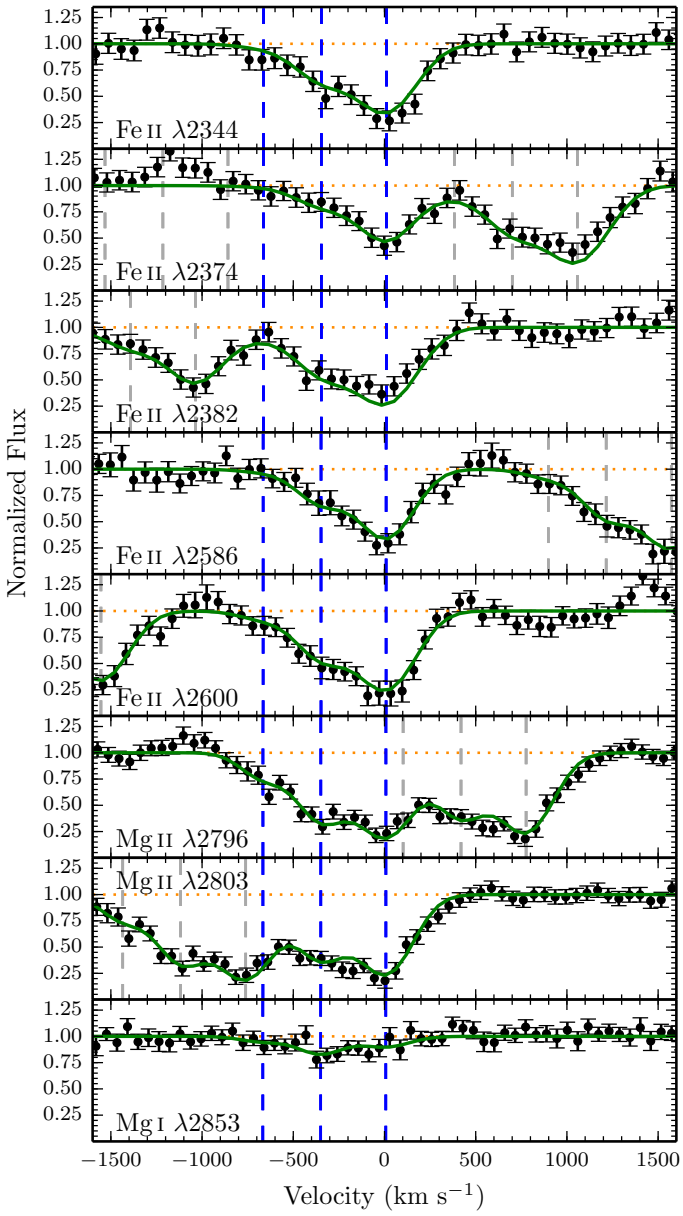

Fig. 2. Fe II, Mg II, and Mg I transitions detected in absorption in the 1D MUSE spectrum. Error bars show the 1σ error on the flux (black), and the green curve traces the fit to the absorption profiles. Zero velocity is relative to the galaxy systemic redshift, $z = 1.2902$. Vertical blue dashed lines mark the three components used to fit each absorption, and gray dashed lines show components that are part of neighboring transitions. The asymmetric absorption profiles indicate significant blue-shifted absorption.

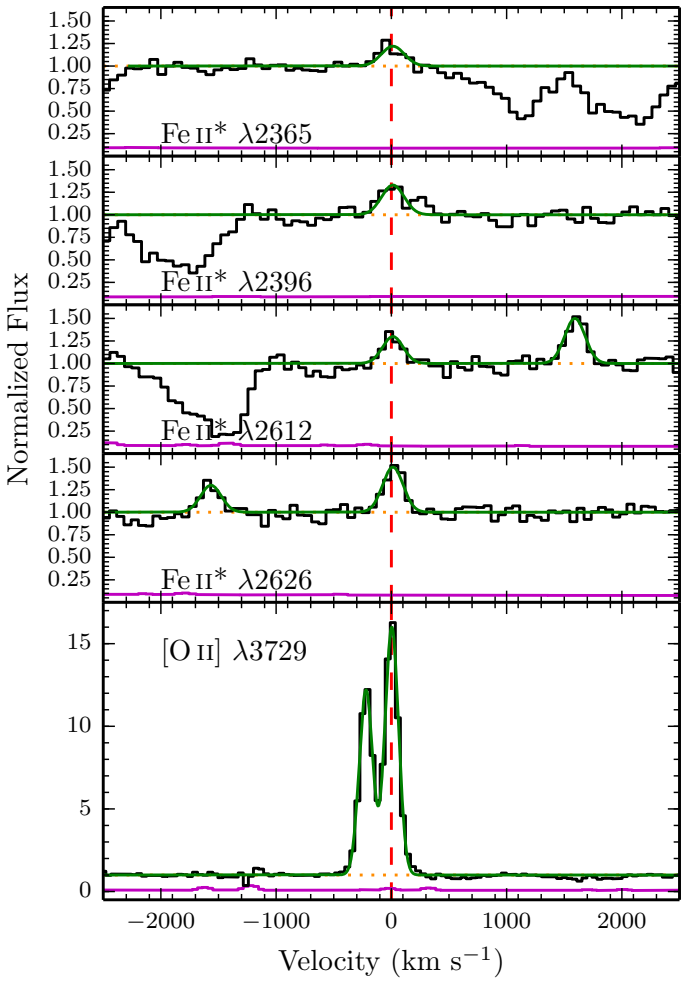

Fig. 3. Fe II* and [O II] emission peaks detected in the normalized 1D MUSE spectrum. The green curve traces joint Gaussian fits to the four Fe II* emission peaks and the [O II] doublet, respectively. Zero velocity, indicated with the vertical red dashed line, is relative to the galaxy systemic redshift, $z = 1.2902$, measured from the [O II] emission.

5. Morphology of the Fe II* emission

In this section, we investigate whether the Fe II* emission has a similar spatial extent and morphology as the stellar continuum and the [O II] $\lambda\lambda 3727, 3729$ emission.

For the Fe II* emission, first we produced a sub-cube of size $1.5'' \times 1.5''$ for each of the four emission lines and transformed the wavelength axis to velocity space. We interpolated each sub-cube to the same velocity scale with pixels of 30 km s^{-1} that span ± 930 km s^{-1} and zero velocity at the galaxy systemic redshift, $z = 1.2902$.

We subtracted the continuum and combined the four sub-cubes. To estimate the stellar continuum, we used the mean value from two regions redwards of the Fe II* emission peaks at $\sim\lambda 2425$ Å and $\sim\lambda 2700$ Å that span 115 Å and 300 Å respectively. The continuum pseudo narrowband (NB) image shown in Fig. 4 (middle left) is from the mean of these two continuum regions, which have a flat slope.

From the combined Fe II* emission velocity cube, we then extracted a NB image by summing 13 pixels (± 390 km s^{-1}). The top left panel of Fig. 4 shows the pseudo-narrowband Fe II* image with 2×2 smoothing and without a S/N threshold, which we use for the 2D analysis. For comparison, we also tested an automated extraction with the CubExtractor software (Cantalupo et al., in prep.), shown in Fig. 5, which selects connected volume pixels (voxels) that are above a specified S/N threshold (2.7 was optimal in this case) to produce optimally extracted images, as in Borisova et al. (2016). Our morphological results are independent of the method used to produce the Fe II* NB image.

Similarly, we created the [O II] pseudo-narrowband image from a 30×30 pixel ($1.5'' \times 1.5''$) sub-cube that spans 18 spectral pixels (22.5 Å) to cover the $\lambda\lambda 3727, 3729$ doublet. Again, we subtracted the continuum estimated between ~3550–3600 Å to obtain the [O II] surface brightness map shown in the bottom left panel of Fig. 4.

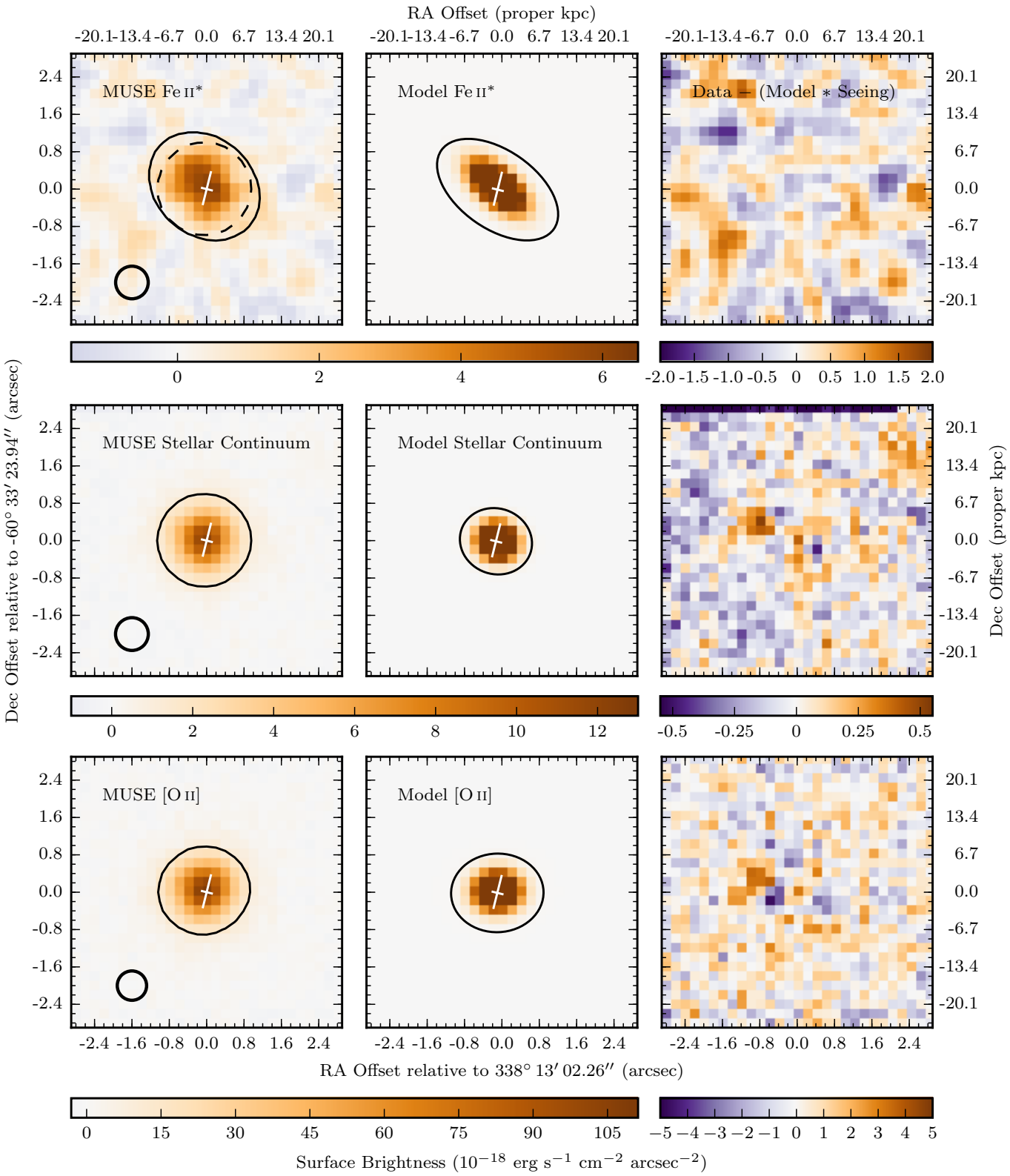

Fig. 4. *Left panels*: Surface brightness maps of Fe II* (*top*), stellar continuum (*middle*), and [O II] emission (*bottom*) from pseudo narrowband images (see text). Solid contours represent 1/10 of the maximum surface brightness. The dashed line in the top left panel corresponds to the stellar continuum contour from middle left panel. The small black circles represent the seeing at the emission wavelength. *Middle panels*: Surface brightness maps of the intrinsic emission from an exponential disk model "deconvolved" from the seeing. Ellipses in the middle column are drawn using the model parameters and have a size that corresponds to the half-light radii (see Table 4). *Right panels*: Maps of the residuals between the observed data and the intrinsic model convolved with the seeing. In the left and middle panels, white crosses indicate the galaxy major and minor axes from the Contini et al. (2016) kinematic analysis. The Fe II* emission map is more extended than both the stellar continuum or the [O II] emission.

Table 3. Emission and absorption rest-frame equivalent width and flux values.

Multiplet	λ Å	E_{high} cm^{-1}	E_{low} cm^{-1}	J	A_{ul} s^{-1}	W_0 Å	Flux 10^{-18} erg s^{-1} cm^{-2}
(1)	(2)	(3)	(4)	(5)	(6)	(7)	(8)
	2600.17	38458.98	0.00	9/2←9/2	Absorption	4.28 ± 0.25	...
	2626.45	38458.98	384.79	9/2→7/2	3.41E+07	−0.93 ± 0.13	2.67 ± 0.43
Fe II UV1	2586.65	38660.04	0.00	7/2←9/2	Absorption	3.14 ± 0.26	...
	2612.65	38660.04	384.79	7/2→7/2	1.23E+08	−0.53 ± 0.15	1.47 ± 0.49
	2632.11	38660.04	667.68	7/2→5/2	6.21E+07	> − 0.27	<0.78 ± 0.42
	2382.76	41968.05	0.00	11/2←9/2	Absorption[a]	3.27 ± 0.22	...
Fe II UV2	2374.46	42114.82	0.00	9/2←9/2	Absorption	2.20 ± 0.22	...
	2396.36	42114.82	384.79	9/2→7/2	2.67E+08	−0.84 ± 0.17	2.37 ± 0.49
	2344.21	42658.22	0.00	7/2←9/2	Absorption	3.47 ± 0.24	···
Fe II UV3	2365.55	42658.22	384.79	7/2→7/2	5.90E+07	−0.42 ± 0.15	1.22 ± 0.48
	2381.49	42658.22	667.68	7/2→5/2	3.10E+07[b]	···	···
	2324.21	43025.3	0.00	3/2→1/2	...		
	2325.40	43003.3	0.00	1/2→1/2	...		
C II]	2326.11	43053.6	63.42	5/2→3/2	...	−1.03 ± 0.18	2.83 ± 0.50
	2327.64	43025.3	63.42	3/2→3/2	...		
	2328.83	43003.3	63.42	1/2→3/2	...		
[O II]	3727.10	26830.57	0.00	3/2 →3/2	...	−48.98 ± 0.29	133.46 ± 0.80
	3729.86	26810.55	0.00	5/2 →3/2	...		

Notes. Column (1): transition name. Column (2): transition wavelength. Column (3): upper energy level. Column (4): lower energy level. Column (5): level total angular momentum quantum number J. Column (6): einstein A_{ul} coefficient for spontaneous emission. Column (7): rest-frame equivalent width. Column (8): line flux. [(a)] Fe IIλ2382 is a pure resonant transition with no associated Fe II* emission. [(b)] Fe II*λ2381 emission is blended with Fe IIλ2382 absorption.

The Fe II* map in Fig. 4 is the first 2D spatial map of the Fe II* non-resonant emission in a individual galaxy at intermediate redshift. Previous studies have searched for signatures of extended Fe II* emission in stacked spectra (Erb et al. 2012; Tang et al. 2014). In a stacked spectrum from 95 star-forming galaxies at $1 < z < 2$, Erb et al. (2012) found that the Fe II* λ2626 emission line is slightly more spatially extended that the stellar continuum. Tang et al. (2014) performed a similar analysis with 97 star-forming galaxies at $1 \lesssim z \lesssim 2.6$, but were not able to spatially resolve the Fe II* emission.

Thanks to the sensitivity of MUSE, we are able to address whether Fe II* is more extended than the continuum and to characterize the Fe II* emission morphology for the first time. The top left panel of Fig. 4 shows that the extended Fe II* emission appears to be more extended than the continuum and has a privileged direction. Comparing the Fe II* emission position angle with the kinematic axis of the galaxy shows that the Fe II* is more extended along the minor kinematic axis of the galaxy.

To quantify the extent of the Fe II*, stellar continuum, and [O II] $\lambda\lambda$3727, 3729 emission, we used a custom Python MCMC algorithm to fit each of the surface brightness maps in the left column of Fig. 4 with a Sersic profile. The fit provides us with intrinsic parameters and with an intrinsic model of the emitting region, that is, deconvolved from the seeing, because we convolve the Sersic profile with the actual PSF taken from the brightest star in the same data cube, MUSE HDFS ID#1 (see Bacon et al. 2015), across wavelengths corresponding to the galaxy emission lines[5]. In practice, we fix the Sersic index n to $n = 1$ or $n = 0.5$ because the Sersic index n is unconstrained[6]. The size estimate, $R_{1/2}$, is nonetheless robust and independent of the Sersic index n, since it is determined empirically from the flux growth curve, an integrated quantity.

Table 4. Summary of 2D morphological analysis.

	Fe II*	Stellar continuum	[O II]
Axis ratio	0.57 ± 0.01	0.90 ± 0.02	0.85 ± 0.01
$R_{1/2}$ (arcsec)	0.49 ± 0.05	0.28 ± 0.02	0.33 ± 0.02
$R_{1/2}$ (kpc)	4.1 ± 0.4	2.34 ± 0.17	2.76 ± 0.17

Table 4 summarizes the results from this analysis and Fig. 4 (middle column) shows the modeled profiles for $n = 1$ for the Fe II*, stellar continuum, and [O II] emission. The right column of Fig. 4 gives the residual maps, which are the difference between the observed data and the intrinsic model convolved with the seeing.

The stellar continuum emission (Fig. 4, middle row) appears round and compact. The intrinsic emission from the exponential disk fit yields an inclination of 28 ± 3° and a half-light radius, $R_{1/2}$, of around 0.28 ± 0.02″ (2.34 ± 0.17 kpc). These continuum emission properties from MUSE are comparable to the measurements from HST images discussed in Sect. 3 and shown in Table 1. The [O II] $\lambda\lambda$3727, 3729 emitting region has the same morphology but is slightly more extended than the stellar continuum with $R_{1/2,[OII]} = 0.33 \pm 0.02''$ (2.76 ± 0.17 kpc).

[5] The PSF can be approximately described by a Moffat profile with FWHM 0.70″ (0.63″) at the Fe II* and stellar continuum emission ([O II] emission) wavelengths, which corresponds to a half-light radius of 0.50″ (0.44″).

[6] The Sersic n index is unconstrained because the seeing radius is much larger than the emission. Indeed, the seeing radius is $FWHM/2 = 0.35''$, corresponding to $R_{1/2} \approx 0.5''$ for a Moffat profile, whereas the galaxy's intrinsic half-light radius $R_{1/2}$ is only ≈0.3″.

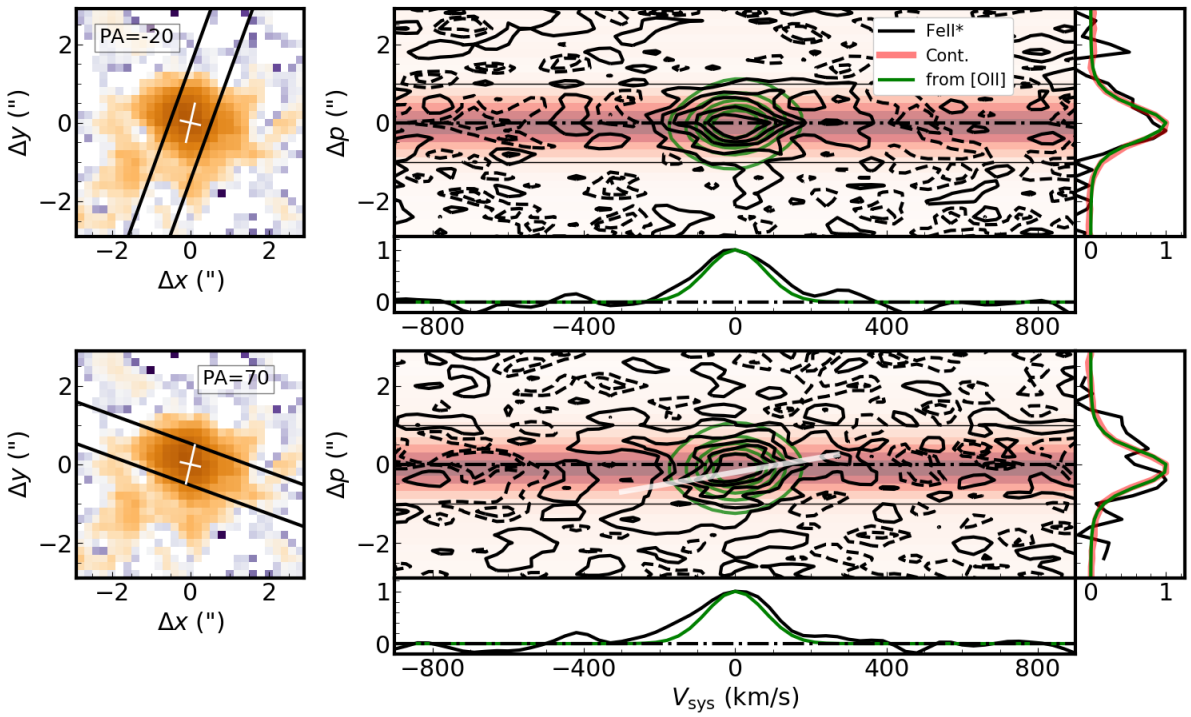

Fig. 5. *Left panels*: narrowband images of the Fe II* emission optimally extracted from the MUSE cube shown with a 1″-wide slit oriented −20° (*top*) and +70° (*bottom*). The +70° slit orientation in the *bottom panels* follows the Fe II* major kinematic axis. The white crosses indicate the galaxy major and minor axes from the Contini et al. (2016) kinematic analysis of [O II]. *Right panels*: position-velocity diagrams of the Fe II* emission from a slit oriented −20° (*top*) and +70° (*bottom*). Zero velocity is relative to the galaxy systemic redshift, z =1.29018 ± 0.00006, measured from the [O II] emission. Solid black contours trace Fe II* flux levels at 1.2, 3.6, 6, 8.4, and 11 × 10^{-20} erg s^{-1} cm^{-2}. Dashed black contours show the negative flux levels at –1.2 and –2.4 ×10^{-20} erg s^{-1} cm^{-2}. Green contours represent the ISM component estimated from [O II] (see text). The red gradient indicates the continuum intensity. The right side panel of each $p - v$ diagram compares the spatial profile of the Fe II* emission (black) with that of the stellar continuum (red) and the ISM component (green). The *bottom sub-panel* of each $p - v$ diagram shows the total 1D flux spectrum integrated across the spatial region between −1″ and +1″ in the $p - v$ diagram with the Fe II* emission in black and the [O II] emission in green. In the *bottom* $p - v$ diagram, the white solid line follows the velocity gradient. This panel also reveals a "C"-shape pattern in the blue wing of the Fe II* emission extending to –400 km s^{-1}. The blue wing of the Fe II* emission is more pronounced along the slit orientation corresponding to the minor-axis (PA = +70°), whereas the red wing appears for both slit orientations.

The corresponding star formation rate surface density is Σ_{SFR} = 1.6 $M_\odot$ kpc^{-2}.

The Fe II* emission has a morphology and physical extent that are different from the stellar continuum and [O II] emission. The intrinsic Fe II* emission is more elliptical with an axis ratio of b/a = 0.57, compared to the rounder continuum and [O II] emission, which both have $b/a \simeq 0.9$. The Fe II* emission is elongated along the direction (PA ≈ +60°) that roughly corresponds to the galaxy minor kinematic axis (PA ≈ +75°, Table 1). Moreover, the intrinsic half-light radius of the Fe II* emission is $R_{1/2,\,\mathrm{Fe\,II*}}$ = 0.49 ± 0.05″, that is, about 50% larger than that of the stellar continuum. In other words, the Fe II* half-light radius, $R_{1/2,\,\mathrm{Fe\,II*}}$ = 4.1 ± 0.4 kpc, extends ≳1.5 kpc beyond the stellar continuum and the [O II] emission, which both have $R_{1/2} \approx 2.5$ kpc (Table 4). This is apparent from comparing the extent of the Fe II* emission to the continuum emission in the top left panel of Fig. 4. See Table 4 for the emission properties.

6. Kinematics of the Fe II* emission

In this section, we investigate whether it is possible to trace the kinematics of the Fe II* emission. To do so, we visually inspected the velocity cube produced in the previous section and found that the kinematic major axis from the Fe II* emission follows a PA of about +70°, which happens to roughly correspond to the galaxy minor kinematic axis. Figure 5 shows $p - v$ diagrams for this +70° slit orientation (bottom row) and for a slit oriented at −20° (top row). In both cases, the slit width is 1″. Following the peak of the Fe II* emission, we see that the Fe II* emission has a velocity gradient along the galaxy minor kinematic axis. This velocity gradient is indicated in the bottom $p - v$ diagram. Figure 5 also indicates the ISM component of the Fe II* emission, estimated by using the parameters from a 2D fit to the [O II] doublet to produce a single Guassian emission line scaled to the maximum intensity of the Fe II* emission.

Comparing the contours for the ISM component and the total Fe II* emission in the $p - v$ diagrams, we see that the Fe II* emission is kinematically more extended than the ISM component, with both red and blue wings. The red wing of the Fe II* emission extends to around +300 km s^{-1} and is noticeable in the $p - v$ diagrams from both slit orientations. For the slit orientation of +70°, the blue wing of the Fe II* emission extends to −400 km s^{-1} near +1″ and −1.5″, decreasing to −200 km s^{-1} in between, and forms a C-shaped pattern. The red and blue wings suggest a bi-conical outflow and the C-shape pattern could motivate a hollow conical geometry.

Figure 6 shows the spatial distribution of the Fe II* emission from the blue-shifted (left) and redshifted (right) components

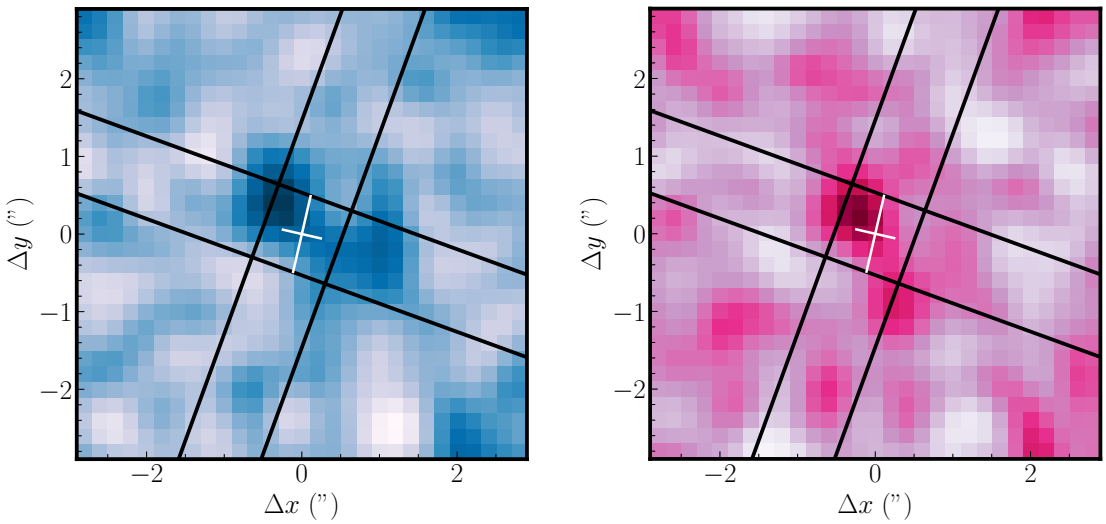

Fig. 6. Maps of the Fe II* emission from the blue-shifted (*left*) and redshifted (*right*) outflow components with 2 × 2 Gaussian smoothing. The black lines show the two slit positions at +70°, and −20°. The white crosses indicate the galaxy major and minor axes from the Contini et al. (2016) kinematic analysis of [O II]. The strongest emission from both the red and the blue-shifted components is roughly spatially coincident. In the case of a bi-conical outflow, this suggests that we may be observing emission predominantly from the base of the wind, not far from the plane of the galaxy.

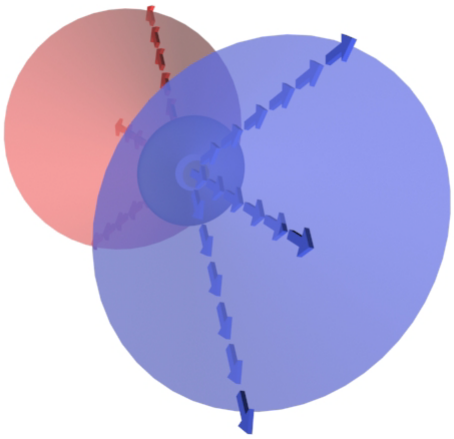

Fig. 7. Schematic representation of a bi-conical outflow from the minor axis of a nearly face-on galaxy.

of the outflow after subtracting the ISM component. The Fe II* emission from the blue and redshifted components is roughly spatially coincident. In the case of a bi-conical outflow, this suggests that we may be observing emission predominantly from the base of the wind, not far from the plane of the galaxy. Figure 7 presents a schematic representation to visualize a bi-conical outflow from a nearly face-on galaxy.

7. Discussion

From deep MUSE observations of the HDFS, we identify a spatially-resolved galaxy (ID#13) at $z = 1.2902$ that has a low inclination ($i = 33°$), an orientation that may favor detecting galactic outflows in emission (Rubin et al. 2014). This galaxy has a star formation rate of $SFR = 77^{+40}_{-25}\ M_\odot\ \mathrm{yr}^{-1}$, which places it in the starburst category (see Contini et al. 2016, their Fig. 3). Its star formation rate surface density $\Sigma_{\mathrm{SFR}} = 1.6\ M_\odot\ \mathrm{kpc}^{-2}$ is well above the threshold for galactic winds (Newman et al. 2012; Bordoloi et al. 2014). The star formation rate and stellar mass of the HDFS galaxy ID#13 are nearly identical to those of two other published individual galaxies with non-resonant Fe II* emission at $z = 0.694$ (Rubin et al. 2011) and $z = 0.9392$ (Martin et al. 2013).

The two galaxies from Rubin et al. (2011) and Martin et al. (2013), like the HDFS galaxy ID#13, also show direct evidence of galactic winds from blue-shifted absorptions. Neither the HDFS galaxy ID#13 nor these two galaxies have Fe II P-Cygni profiles, although they might have moderate resonant Fe II emission infilling. The HDFS galaxy ID#13 differs from the these galaxies in that it lacks any obvious Mg II emission, whereas the Rubin et al. (2011) and Martin et al. (2013) galaxies have strong Mg II P-cygni profiles. Among composite spectra that detect non-resonant Fe II* emission (Talia et al. 2012; Erb et al. 2012; Kornei et al. 2013; Tang et al. 2014; Zhu et al. 2015), only the galaxy samples from Erb et al. (2012) and Kornei et al. (2013) reveal Mg II P-cygni profiles.

Our analysis of the HDFS galaxy ID#13 is the first to spatially map extended Fe II* emission (Sect. 5) around an individual galaxy (Fig. 4). We showed that this Fe II* emission is also kinematically extended (Fig. 5) with blue-shifted emission (extending to −400 km s^{-1}) and redshifted emission (extending to +350 km s^{-1}). The blue-shifted emission forms a C-shaped pattern, suggesting a bi-conical outflow (Fig. 7). Furthermore, the strong, asymmetric Fe II and Mg II absorptions in the 1D galaxy spectrum, which have blue-shifted components at −660 km s^{-1} and −350 km s^{-1} relative to the systemic redshift (Fig. 2), are also a clear signature of outflowing gas. In Sect. 7.2, we will estimate the mass outflow rate and compare it to the galaxy SFR.

First, in Sect. 7.1, we compare the absorption and emission properties from the HDFS galaxy ID#13 and the two other individual galaxies with predictions from radiative transfer wind models.

7.1. Comparison with radiative transfer models

The MUSE surface brightness maps (Fig. 4) reveal that the Fe II* emission has a more elliptical shape than the stellar continuum and the [O II] emission. Along with the kinematic signatures discussed in the previous section (Fig. 5), this indicates that the

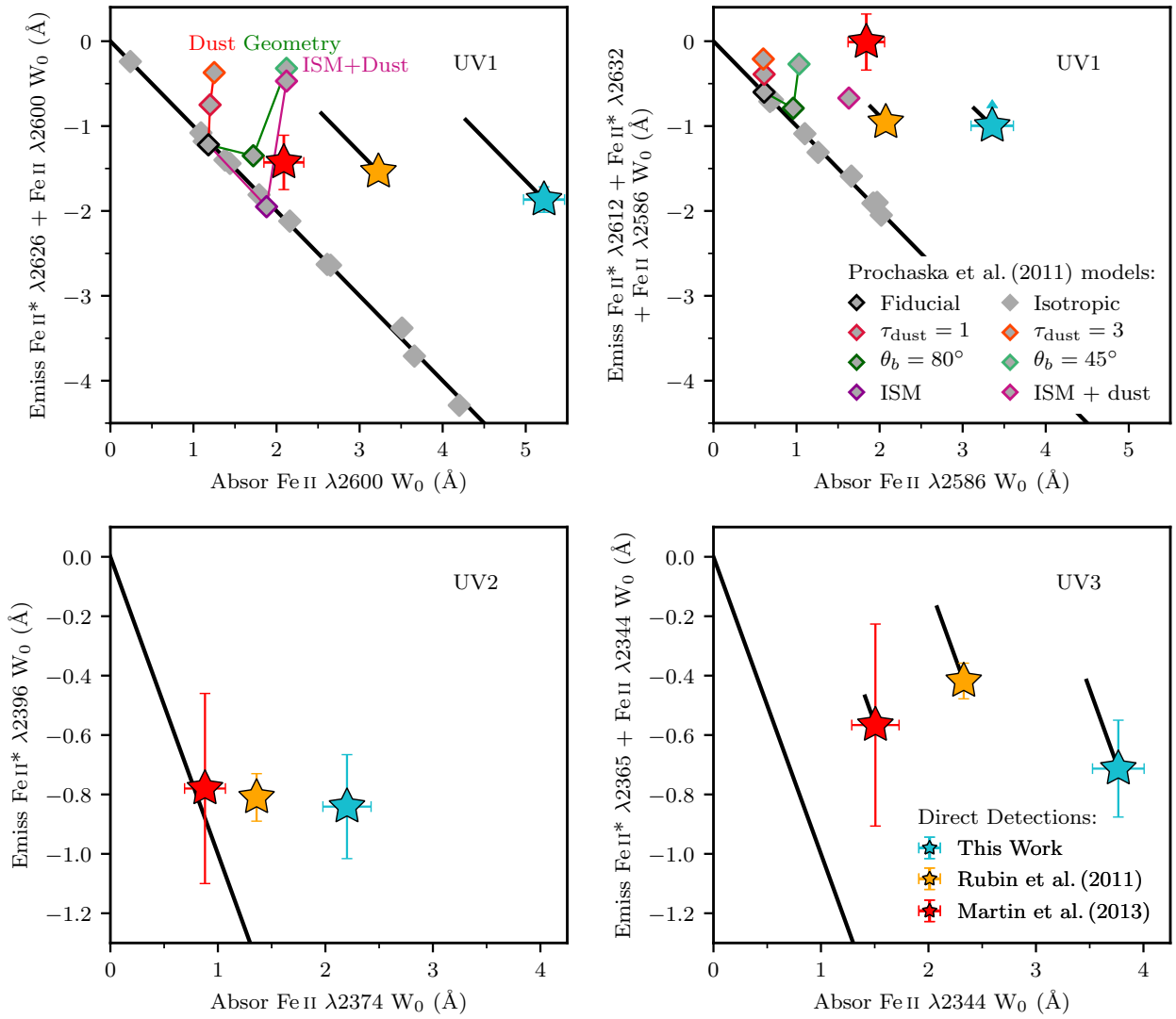

Fig. 8. Comparison of observed and modeled rest-frame equivalent widths from the Fe II UV1, UV2, and UV3 multiplet transitions. Each panel plots the total equivalent width from re-emission as a function of the corresponding resonant absorption equivalent width. The black diagonal "photon-conservation" line indicates equal amounts of absorption and re-emission. Star-shaped points show the infilling-corrected equivalent width values from three direct detections: this work (blue), Rubin et al. (2011; yellow), and Martin et al. (2013; red). The diagonal black lines associated with these points trace the infilling correction. Gray diamonds in the top panels come from radiative transfer model predictions for the UV1 multiplet (Prochaska et al. 2011). Diamonds with colored outlines represent variations to the fiducial isotropic outflow model (black outline) that move the model predictions away from the photon-conservation line. Model predictions for the Fe II UV2 and UV3 multiplets are not currently available.

emission is not isotropic. Isotropic outflows are, however, the fiducial geometry for radiative transfer and semi-analytic wind models (Prochaska et al. 2011; Scarlata & Panagia 2015)[7].

Another notable difference is that the Prochaska et al. (2011) models of galactic outflows all predict resonant Fe II P-Cygni profiles, whereas none of the observations of Fe II* emitters, whether in individual (HDFS galaxy ID#13, Rubin et al. 2011; Martin et al. 2013) or composite spectra (Talia et al. 2012; Erb et al. 2012; Kornei et al. 2013; Tang et al. 2014; Zhu et al. 2015), show Fe II P-cygni profiles.

Prochaska et al. (2011) produce models for the Fe II UV1 multiplet and Mg II $\lambda\lambda$2797, 2803 doublet to explore how varying model geometries and physical assumptions about the dust content, ISM contribution, gas density, and wind speeds impact the line profiles from the resonant and non-resonant transitions. Varying each of the physical properties individually from the fiducial model is not sufficient to suppress the resonant Fe II and Mg II P-Cygni profiles, and the only model that substantially suppresses the resonant emission combines an ISM component with dust extinction.

We have compared the emission and absorption properties of the MUSE HDFS galaxy ID#13 with predictions from the Prochaska et al. (2011) radiative transfer models, following Erb et al. (2012). In Fig. 8, we show the total amount of emission (from both resonant and non-resonant channels) versus the total amount of resonant absorption for the Fe II UV1, UV2, and UV3 multiplets. Absorptions from the Fe II λ2600 (UV1), Fe II λ2586 (UV1), Fe II λ2374 (UV2), and Fe II λ2344 (UV3) resonant transitions (clockwise from upper left) can each lead to non-resonant Fe II* re-emission and are presented in the four panels (clockwise from the upper left). The total re-emission includes more or less resonant emission infilling, depending on

[7] These models can be adapted to explore how the absorption and emission line profiles vary for different anisotropic configurations.

the Einstein A coefficients for the transitions (Tang et al. 2014; Zhu et al. 2015). For example, ~90% of the re-emission following Fe II λ2374 absorption is re-emitted as Fe II* λ2396 non-resonant emission, making the emission infilling negligible.

In Fig. 8, we also include the two previously published direct detections of Fe II* emission from individual star-forming galaxies (Rubin et al. 2011; Martin et al. 2013). Along with the points for the three direct detections of Fe II* emission, we plot lines that represent the emission infilling correction. We applied the emission infilling correction following the method from Zhu et al. (2015) described in Sect. 4.1. This correction shifts the observed points parallel to the "photon-conservation" line that indicates equal amounts of absorption and re-emission in each panel. For the most part, the three direct detections have similar amounts of total emission, but their absorption equivalent widths span a larger range of values.

The top panels of Fig. 8 show the Prochaska et al. (2011) model predictions for the UV1 multiplet. The majority of the models are isotropic with no dust extinction, and they follow the photon-conservation line. These models modify the gas density and velocity laws characterizing the outflow. The models that depart from the photon-conservation line include dust extinction or geometry variations. The effects of dust and geometry are more noticeable for the FeII λ2600 transition than the FeII λ2586 transition, because the Fe II λ2600 transition is more likely to scatter resonantly multiple times (Fig. 5 of Tang et al. 2014), amplifying the effects of dust and geometry.

To gain physical intuition for the impact of the individual properties, we now discuss how varying the outflow geometry, dust extinction, and ISM component affects the total emission and absorption budget. To identify the impact of a bi-conical outflow geometry, we compared the fiducial isotropic model (black outlined diamond in Fig. 8) with two bi-conical outflow models, where the wind fills an opening angle of, respectively, 80° and 45° (green outlined diamonds) along the line of the sight to the galaxy. Collimating the outflow suppresses both the resonant and non-resonant emission, and for highly collimated outflows, absorption dominates the profile. From these two bi-conical outflow models, a trend in how the total emission changes with the opening angle is not clear.

Comparing models that include dust in an isotropic outflow (red-orange outlined diamonds in Fig. 8) to the fiducial model shows that dust extinction has a strong impact only on the total emission. Increasing the amount of dust extinction moves the points nearly vertically off of the photon-conservation line, since more re-emitted photons can be absorbed by dust. Dust extinction suppresses the resonant emission slightly more than the non-resonant emission.

Adapting the fiducial model to include an ISM component, that is, centralized gas that lacks a significant radial velocity, simply increases the amount of gas that can absorb and re-emit photons. The point representing this model (dark purple outlined diamond in Fig. 8) stays on the photon-conservation line, since neither the ISM component nor the wind component contains dust[8]. Adding the ISM component produces absorption around zero systemic velocity and allows more photons to escape through non-resonant re-emission. The ISM component suppresses the resonant Fe II emission, while boosting the non-resonant Fe II* emission, each by a factor of about four compared to the fiducial model. Including an ISM component is essential to re-creating the observations from the galaxy ID#13.

Finally, Prochaska et al. (2011) include dust extinction ($\tau_{\rm dust}$ = 1) in the ISM component, which again shifts the point representing this model (magenta outlined diamond in Fig. 8) nearly vertically from the photon-conservation line. Compared to the dusty wind-only model discussed earlier, this model suffers much more from dust extinction because the simple kinematic structure of the ISM allows multiple scattering events. Although both the resonant and non-resonant emission lines diminish compared to the ISM model without dust, the ratio between the Fe II* emission and Fe II emission still remains stronger than in the fiducial model. Adapting the ISM+dust model to match the total absorption from the galaxy ID#13 would be an interesting comparison.

In summary, collimating a bi-conical outflow or increasing the amount of dust extinction both produce more absorption than emission, shifting the model predictions away from the photon conservation line. For dust extinction, the shift is nearly vertical, affecting primarily the total amount of emission. For a bi-conical outflow, the amount of absorption also increases, although more models would be beneficial to determine how emission varies with opening angle. An ISM component is essential to favor non-resonant emission, suppress resonant emission that creates Fe II P-cygni profiles, and produce line profiles that are qualitatively similar to observations.

The observed galaxies with Fe II* emission are all offset from the photon conservation line and also do not coincide with the model predictions. Model predictions for the UV2 and UV3 multiplets would be useful to compare with the observations and confirm how physical effects impact the absorption and emission equivalent widths. Models combining multiple physical effects, such as the ISM+dust model for UV1, are necessary to re-produce the observations. For the HDFS galaxy ID#13, we suggest that a model combining a dusty ISM with a bi-conical outflow (motivated by our morphological and kinematic observations) would be able to match the data for the HDFS galaxy ID#13. Such a model would address the isotropic outflow geometry and Fe II P-cygni profiles that the observations do not support.

7.2. Mass outflow rate estimation

To estimate the mass entrained in the outflow, we consider only the absorption components that are not affected by the ISM. Consequently, we exclude the component "C" at the systemic velocity (Fig. 2, Table 2). The other two components are blue-shifted by −660 km s^{-1} ("A") and −350 km s^{-1} ("B"), respectively. The wind component "B" at −350 km s^{-1} dominates the bulk of the mass flux given the equivalent width ratios between components "A" and "B". As discussed in Sect. 4.1, the wind component 'B' is the least affected by emission infilling (at or below the 10% level), whereas the ISM component "C" is the most affected by emission infilling. Hence, emission infilling does not affect our estimate of the mass outflow rate from the wind component "B".

Similar to Rubin et al. (2014), we estimate the mass outflow rate from

$$\frac{{\rm d}M}{{\rm d}t} \approx 1\ M_\odot\ {\rm yr}^{-1} C_f \frac{N_{\rm flow}({\rm H})}{10^{20}\ {\rm cm}^{-2}} \frac{A_{\rm flow}}{45\ {\rm kpc}^2} \frac{v}{300\ {\rm km\ s}^{-1}} \frac{5\ {\rm kpc}}{D} \quad (1)$$

where $C_{\rm f}$ is the covering fraction of the outflowing gas, $N_{\rm flow}$(H) is the column density of hydrogen associated with the outflow, $A_{\rm flow}$ is the projected surface area of the outflow, v is the outflow

[8] The Fe II λ2586 panel does not have a point for the ISM model, because no values are given for the resonant re-emission in Table 2 of Prochaska et al. (2011).

velocity, and D is the physical distance the outflow extends from the galaxy center.

We estimate $N_{\rm flow}$(H) from the metal column densities N(Fe) and N(Mg). Because VPFIT column densities and Doppler b parameters are degenerate for optically thick lines, we determine the metal column densities N(Fe) and N(Mg) from the equivalent width, W_0, following Spitzer (1968), with an additional term for the covering fraction:

$$\log N = \log\frac{W_0}{\lambda} - \log\frac{2F(\tau_0)}{\pi^{1/2}\tau_0} - \log \lambda f - \log C_{\rm f} + 20.053 \qquad (2)$$

where τ_0 is the optical depth at line center, λ is the transition wavelength in Å, and f is the oscillator strength. The optical depth τ_0 is determined from the ratio of equivalent widths from two lines within the same multiplet, as in Weiner et al. (2009) and Rubin et al. (2010b), which is referred to as the "doublet ratio" method.

For Mg II, the oscillator strengths indicate that the equivalent width ratio is 2:1 in the optically thin case. The Mg II equivalent width ratio follows $F(2\tau_0)/F(\tau_0)$ for the transmission integral:

$$F(\tau_0) = \int_0^{+\infty} (1 - {\rm e}^{-\tau_0\ \exp(-x^2)}){\rm d}x. \qquad (3)$$

From our measured Mg II equivalent width ratio, 1.06 ± 0.13, we numerically solve for $\tau_{0,2803} \approx 240$. Both the equivalent width ratio and the high optical depth value indicate that Mg II is saturated.

For Fe II, we can calculate the optical depth for two different sets of transitions: $\tau_{0,2586}$ from $W_{0,2600}/W_{0,2586}$ and $\tau_{0,2374}$ from $W_{0,2382}/W_{0,2374}$. The optical depth ratios are 3.46:1 and 10.22:1 respectively, using the oscillator strength values from Morton (2003). After again solving numerically, the optical depth values are $\tau_{0,2586} = 3.53$ and $\tau_{0,2374} = 1.55$. We can therefore use these optical depth and equivalent width values to obtain a good estimate of the Fe II column density, since Jenkins (1986) find accurate column densities even for blended components that result from multiple clouds, as long as the optical depth in the weaker transition is $\tau_0 < 5$.

With knowledge of the optical depth, we can determine the covering fraction from the residual intensities between the zero level and the doublet lines (Rupke et al. 2005; Sato et al. 2009; Martin & Bouché 2009; Martin et al. 2012; Rubin et al. 2014). Using Eq. (5) from Rupke et al. (2005) with Mg II, we find a covering fraction of at least 0.4. However, this formula ignores the instrument resolution, which could lead to a much higher covering fraction. To estimate a lower limit on the column density, we take $C_{\rm f} = 1$, as in Rubin et al. (2010b).

Applying Eq. (2), the column density measurements are N(Mg II λ2803) = 15.89, N(Fe II λ2586) = 14.74, and N(Fe II λ2374) = 14.76. These measurements are in good agreement with the values from vpFit, N(Mg II) = 15.87 ± 0.68 and N(Fe II) = 14.75 ± 0.16.

From the metal column densities, in order to estimate the gas flow column density $N_{\rm flow}$(H), we use solar abundances (with log(Mg/H) = −4.40 and log(Fe/H) = −4.50; Asplund et al. 2009) and a dust depletion correction but no ionization correction, as in Rubin et al. (2011). To estimate the dust depletion factor, we use the Jenkins (2009) method to simultaneously fit for the depletion level using the column densities of these two elements (Mg, Fe). The fit yields a global depletion factor of $F_\star = 1.25 \pm 0.39$, corresponding to δFe of −2.60 dex and δMg of −1.50 dex. With these depletion corrections, the total gas column density is thus at least $\log N({\rm H}) \geq 21.76 \pm 0.48 - \log Z/Z_\odot$, given that we used solar abundances[9].

We can estimate the projected area of the ouflow $A_{\rm flow}$ from the size of the stellar continuum, since we detect Mg II and Fe II in absorption against the continuum. The MUSE stellar continuum (Sect. 5) has an intrinsic half-light radius of 2.34 ± 0.17 kpc. Because the spectrum is optimally extracted with a white-light image weighting scheme, the effective half-light radius of the extracted 1D spectrum is $R_{1/2,\rm eff} = \sqrt{2} \times R_{1/2,\star}$ or 3.3 kpc. The stellar continuum therefore covers a surface area of $A_{\rm flow} = \pi R^2_{1/2,\star} b/a = 30$ kpc^2.

Finally, we must assume an effective or characteristic distance for the gas at −350 km s^{-1} with a total column density of $\log N_{\rm flow}(H) > 21.80$. For a mass-conserving flow, the gas closer to the galaxy will dominate the column density. However, outflowing gas moving at −350 km s^{-1} needs a few kpc (1−5) to accelerate to that speed (Murray et al. 2011). Hence, we conservatively use an upper limit of $D < 5$ kpc, as in Rubin et al. (2014), which leads to an outflow rate of >45 $M_\odot$ yr^{-1}. For plausible values of 2−3 kpc, the outflow rate would be 75−110 $M_\odot$ yr^{-1}. In comparison, the Fe II* emission has a characteristic size of ∼4 kpc. Overall, the outflow rate is comparable to the star formation rate of 78 $M_\odot$ yr^{-1}.

8. Conclusions

The direct detection of Fe II* emission from the spatially-resolved MUSE HDFS galaxy ID#13 at $z = 1.29$ opens a new avenue for studying galactic outflows in emission. From an analysis of the deepest MUSE field so far (27 h), the properties of this individual galaxy, including the inclination, stellar mass, star formation rate, and gas kinematics, are well characterized (Table 1). This galaxy has a low inclination ($i \sim 33$ deg), $M_\star = 8\times10^9$ $M_\odot$, and $SFR = 77^{+40}_{-25}$ $M_\odot$ yr^{-1}.

Using the 1D integrated spectrum and 2D pseudo-narrowband images, we identified signatures of winds in emission and absorption from the Fe II*, Fe II, and Mg II transitions and investigated the wind morphology and extent. Specifically, we found:

- The SFR surface density from [O II] $\lambda\lambda$3727, 3729 is $\Sigma_{\rm SFR} = 1.6$ $M_\odot$ kpc^{-2}, well above the threshold for galactic winds (Newman et al. 2012; Bordoloi et al. 2014).
- Asymmetric Fe II, Mg II, and Mg I self-absorptions in the MUSE 1D spectrum have a strong blue wing that extends beyond −700 km s^{-1}. The profiles are well fit with three components at −660 km s^{-1}, −350 km s^{-1}, and +9 km s^{-1} (Fig. 2). These blue-shifted absorptions indicate outflowing material along the line of sight, and we estimated a mass outflow rate in the range of 45−110 $M_\odot$ yr^{-1}.
- Emission infilling does not appear to significantly impact the absorption profiles because (i) they all have very similar shapes, unlike in Zhu et al. (2015); and (ii) the strongest component for all absorptions (including Fe II λ2600 and λ2382) remains consistent with the galaxy systemic redshift (Fig. 2). A quantitative analysis following the Zhu et al. (2015) empirical method finds that emission infilling could impact the Fe IIλ2600 (Fe IIλ2382) rest-frame equivalent width by at most 22% (55%) and less for the other Fe II transitions. Figure 8 shows how applying the emission infilling

[9] Ionization corrections would further increase the column density, but they are small at this level.

correction impacts the observed rest-frame equivalent width values.

- Non-resonant Fe II* emission from the λ2365, λ2396, λ2612, and λ2626 transitions have fluxes of $1.2-2.4-1.5-2.7 \times 10^{18}$ erg s^{-1} cm^{-2}, respectively, and flux ratios that are consistent with optically thick gas (Tang et al. 2014). The Fe II* λ2632 transition has a 1σ flux limit of $<8 \times 10^{-19}$ erg s^{-1} cm^{-2}. Contrary to stacked spectra (e.g., Zhu et al. 2015), the Fe II* emission in this galaxy appears to be symmetric and well-centered on the galaxy [O II] systemic redshift (Fig. 3).
- After stacking the four non-resonant Fe II* emission lines, we obtain the first spatially-resolved 2D map of this non-resonant emission from a $z \sim 1$ galaxy (Fig. 4). The Fe II* emission is more extended than the stellar continuum or [O II] emission. The Fe II* emission half-light radius is $R_{1/2,\,\mathrm{Fe\,II^*}} = 4.1 \pm 0.4$ kpc, about 70% larger than that of the continuum which has $R_{1/2,\star} = 2.34 \pm 0.17$ kpc. The Fe II* emission also has a different morphology; it is more elongated in the direction that roughly corresponds to the galaxy minor kinematic axis.
- The Fe II* emission displays a velocity gradient along the kinematic minor axis, and the blue wing of the emission contours reveals a C-shape pattern in a $p-v$ diagram from a pseudo-slit extracted along this axis (Fig. 5). These features are consistent with a conical outflow.
- Comparing the observed emission and absorption properties with predictions (Fig. 8) from the radiative transfer models of Prochaska et al. (2011) suggests that the isotropic fiducial wind model fails, but that a bi-conical wind model including a dusty ISM component could more likely reproduce the observations from galaxy ID#13.

This geometry agrees with a growing body of models and observations that suggest outflowing gas driven by supernovae explosions escapes the disk preferentially along the galaxy minor axis in a bi-conical flow (e.g., Chen et al. 2010; Bordoloi et al. 2011; Bouché et al. 2012; Bolatto et al. 2013; Kornei et al. 2013; Kacprzak et al. 2012; Martin et al. 2012; Krips et al. 2016).

Fe II* emission from the MUSE HDFS galaxy ID#13 was identified serendipitously, but by systematically searching through field galaxies in similar IFU data sets it will be possible to construct samples of $z \sim 1$ galaxies that each show evidence of outflows in emission. Observational constraints from these samples can then drive improvements to models of galactic-scale outflows.

Acknowledgements. We thank the anonymous referee for providing useful feedback. This work has been carried out thanks to the support of the ANR FOGHAR (ANR-13-BS05-0010-02), the OCEVU Labex (ANR-11-LABX-0060), and the A*MIDEX project (ANR-11-IDEX-0001-02) funded by the "Investissements d'avenir" French government program. N.B. acknowledges support from a Career Integration Grant (CIG) (PCIG11-GA-2012-321702) within the 7th European Community Framework Program. R.B. acknowledges support from the ERC advanced grant 339659-MUSICOS. J.B. is supported by FCT through Investigador FCT contract IF/01654/2014/CP1215/CT0003, by Fundação para a Ciência e a Tecnologia (FCT) through national funds (UID/FIS/04434/2013), and by FEDER through COMPETE2020 (POCI-01-0145-FEDER-007672). B.E. acknowledges support from the "Programme National de Cosmologie and Galaxies" (PNCG) of CNRS/INSU, France. R.A.M. acknowledges support by the Swiss National Science Foundation. J.R. acknowledges support from the ERC starting grant 336736-CALENDS.

References

Adelberger, K. L., Shapley, A. E., Steidel, C. C., et al. 2005, ApJ, 629, 636
Arribas, S., Colina, L., Bellocchi, E., Maiolino, R., & Villar-Martín, M. 2014, A&A, 568, A14
Asplund, M., Grevesse, N., Sauval, A. J., & Scott, P. 2009, ARA&A, 47, 481
Bacon, R., Brinchmann, J., Richard, J., et al. 2015, A&A, 575, A75
Berry, M., Gawiser, E., Guaita, L., et al. 2012, ApJ, 749, 4
Bolatto, A. D., Warren, S. R., Leroy, A. K., et al. 2013, Nature, 499, 450
Bordoloi, R., Lilly, S. J., Knobel, C., et al. 2011, ApJ, 743, 10
Bordoloi, R., Lilly, S. J., Kacprzak, G. G., & Churchill, C. W. 2014, ApJ, 784, 108
Bordoloi, R., Rigby, J. R., Tumlinson, J., et al. 2016, MNRAS, 458, 1891
Borisova, E., Cantalupo, S., Lilly, S. J., et al. 2016, ApJ, 831, 39
Bouché, N., Hohensee, W., Vargas, R., et al. 2012, MNRAS, 426, 801
Bouché, N., Carfantan, H., Schroetter, I., Michel-Dansac, L., & Contini, T. 2015, AJ, 150, 92
Bouché, N., Finley, H., Schroetter, I., et al. 2016, ApJ, 820, 121
Cazzoli, G., Lattanzi, V., Kirsch, T., et al. 2016, A&A, 591, A126
Cecil, G., Bland-Hawthorn, J., Veilleux, S., & Filippenko, A. V. 2001, ApJ, 555, 338
Cen, R., & Chisari, N. E. 2011, ApJ, 731, 11
Chabrier, G. 2003, ApJ, 586, L133
Chen, Y.-M., Tremonti, C. A., Heckman, T. M., et al. 2010, AJ, 140, 445
Chisholm, J., Tremonti, C. A., Leitherer, C., et al. 2015, ApJ, 811, 149
Cicone, C., Maiolino, R., & Marconi, A. 2016, A&A, 588, A41
Coil, A. L., Weiner, B. J., Holz, D. E., et al. 2011, ApJ, 743, 46
Contini, T., Epinat, B., Bouché, N., et al. 2016, A&A, 591, A49
Diamond-Stanic, A. M., Coil, A. L., Moustakas, J., et al. 2016, ApJ, 824, 24
Dutta, R., Srianand, R., Gupta, N., et al. 2017, MNRAS, 465, 4249
Elbaz, D., Daddi, E., Le Borgne, D., et al. 2007, A&A, 468, 33
Epinat, B., Tasca, L., Amram, P., et al. 2012, A&A, 539, A92
Erb, D. K., Quider, A. M., Henry, A. L., & Martin, C. L. 2012, ApJ, 759, 26
Finlator, K., & Davé, R. 2008, MNRAS, 385, 2181
Fiore, F., Feruglio, C., Shankar, F., et al. 2017, A&A, 601, A143
Ford, A. B., Werk, J. K., Davé, R., et al. 2016, MNRAS, 459, 1745
Förster Schreiber, N. M., Genzel, R., Newman, S. F., et al. 2014, ApJ, 787, 38
Gallerani, S., Pallottini, A., Feruglio, C., et al. 2016, ArXiv e-prints [arXiv:1604.05714]
García-Burillo, S., Combes, F., Usero, A., et al. 2015, A&A, 580, A35
Genzel, R., Newman, S., Jones, T., et al. 2011, ApJ, 733, 101
Heckman, T. M., Dahlem, M., Lehnert, M. D., et al. 1995, ApJ, 448, 98
Heckman, T. M., Alexandroff, R. M., Borthakur, S., Overzier, R., & Leitherer, C. 2015, ApJ, 809, 147
Jaskot, A. E., & Oey, M. S. 2014, ApJ, 791, L19
Jenkins, E. B. 1986, ApJ, 304, 739
Jenkins, E. B. 2009, ApJ, 700, 1299
Kacprzak, G. G., Churchill, C. W., & Nielsen, N. M. 2012, ApJ, 760, L7
Karim, A., Schinnerer, E., Martínez-Sansigre, A., et al. 2011, ApJ, 730, 61
Karman, W., Grillo, C., Balestra, I., et al. 2016, A&A, 585, A27
Kewley, L. J., Geller, M. J., & Jansen, R. A. 2004, AJ, 127, 2002
Kornei, K. A., Shapley, A. E., Martin, C. L., et al. 2012, ApJ, 758, 135
Kornei, K. A., Shapley, A. E., Martin, C. L., et al. 2013, ApJ, 774, 50
Krips, M., Martín, S., Sakamoto, K., et al. 2016, A&A, 592, L3
Laursen, P., Sommer-Larsen, J., & Andersen, A. C. 2009, ApJ, 704, 1640
Lehnert, M. D., Heckman, T. M., & Weaver, K. A. 1999, ApJ, 523, 575
Lilly, S. J., Carollo, C. M., Pipino, A., Renzini, A., & Peng, Y. 2013, ApJ, 772, 119
Martin, C. L., & Bouché, N. 2009, ApJ, 703, 1394
Martin, C. L., Shapley, A. E., Coil, A. L., et al. 2012, ApJ, 760, 127
Martin, C. L., Shapley, A. E., Coil, A. L., et al. 2013, ApJ, 770, 41
Matsubayashi, K., Sugai, H., Hattori, T., et al. 2009, ApJ, 701, 1636
Matsuda, Y., Yamada, T., Hayashino, T., et al. 2012, MNRAS, 425, 878
Moiseev, A., Karachentsev, I., & Kaisin, S. 2010, MNRAS, 403, 1849
Morrissey, P., Matuszewski, M., Martin, C., et al. 2012, in Ground-based and Airborne Instrumentation for Astronomy IV, Proc. SPIE, 8446, 844613
Morton, D. C. 2003, ApJS, 149, 205
Murray, N., Ménard, B., & Thompson, T. A. 2011, ApJ, 735, 66
Newman, S. F., Genzel, R., Förster-Schreiber, N. M., et al. 2012, ApJ, 761, 43
Oppenheimer, B. D., & Davé, R. 2008, MNRAS, 387, 577
Pallottini, A., Ferrara, A., Gallerani, S., Salvadori, S., & D'Odorico, V. 2014, MNRAS, 440, 2498
Peng, C. Y., Ho, L. C., Impey, C. D., & Rix, H.-W. 2002, AJ, 124, 266
Péroux, C., Quiret, S., Rahmani, H., et al. 2016, MNRAS, 457, 903
Prochaska, J. X., Kasen, D., & Rubin, K. 2011, ApJ, 734, 24
Rahmati, A., Schaye, J., Crain, R. A., et al. 2016, MNRAS, 459, 310
Rigby, J. R., Bayliss, M. B., Gladders, M. D., et al. 2014, ApJ, 790, 44
Rubin, K. H. R., Prochaska, J. X., Koo, D. C., Phillips, A. C., & Weiner, B. J. 2010a, ApJ, 712, 574
Rubin, K. H. R., Weiner, B. J., Koo, D. C., et al. 2010b, ApJ, 719, 1503
Rubin, K. H. R., Prochaska, J. X., Ménard, B., et al. 2011, ApJ, 728, 55
Rubin, K. H. R., Prochaska, J. X., Koo, D. C., et al. 2014, ApJ, 794, 156
Rupke, D. S., Veilleux, S., & Sanders, D. B. 2005, ApJS, 160, 87

Rupke, D. S. N., & Veilleux, S. 2015, ApJ, 801, 126
Sato, T., Martin, C. L., Noeske, K. G., Koo, D. C., & Lotz, J. M. 2009, ApJ, 696, 214
Scarlata, C., & Panagia, N. 2015, ApJ, 801, 43
Schroetter, I., Bouché, N., Péroux, C., et al. 2015, ApJ, 804, 83
Schroetter, I., Bouché, N., Wendt, M., et al. 2016, ApJ, 833, 39
Shapley, A. E., Steidel, C. C., Pettini, M., & Adelberger, K. L. 2003, ApJ, 588, 65
Shen, S., Madau, P., Aguirre, A., et al. 2012, ApJ, 760, 50
Shopbell, P. L., & Bland-Hawthorn, J. 1998, ApJ, 493, 129
Silk, J., & Mamon, G. A. 2012, RA&A, 12, 917
Soto, K. T., & Martin, C. L. 2012, ApJS, 203, 3
Spitzer, L. 1968, Diffuse matter in space (New York: Interscience Publication)
Steidel, C. C., Erb, D. K., Shapley, A. E., et al. 2010, ApJ, 717, 289
Steidel, C. C., Bogosavljević, M., Shapley, A. E., et al. 2011, ApJ, 736, 160
Straka, L. A., Johnson, S., York, D. G., et al. 2016, MNRAS, 458, 3760
Talia, M., Mignoli, M., Cimatti, A., et al. 2012, A&A, 539, A61
Tang, Y., Giavalisco, M., Guo, Y., & Kurk, J. 2014, ApJ, 793, 92
Tomczak, A. R., Quadri, R. F., Tran, K.-V. H., et al. 2016, ApJ, 817, 118
Tremonti, C. A., Heckman, T. M., Kauffmann, G., et al. 2004, ApJ, 613, 898
Veilleux, S., & Rupke, D. S. 2002, ApJ, 565, L63
Veilleux, S., Cecil, G., & Bland-Hawthorn, J. 2005, ARA&A, 43, 769
Weiner, B. J., Coil, A. L., Prochaska, J. X., et al. 2009, ApJ, 692, 187
Whitaker, K. E., Franx, M., Leja, J., et al. 2014, ApJ, 795, 104
Wisotzki, L., Bacon, R., Blaizot, J., et al. 2016, A&A, 587, A98
Wood, C. M., Tremonti, C. A., Calzetti, D., et al. 2015, MNRAS, 452, 2712
Zhu, G. B., Comparat, J., Kneib, J.-P., et al. 2015, ApJ, 815, 48